
Optical Properties of Organometallic Perovskite: An *ab initio* Study using Relativistic *GW* Correction and Bethe-Salpeter Equation

TOWFIQ AHMED^{1 (a)}, C. LA-O-VORAKIAT², T. SALIM³, Y. M. LAM³, ELBERT E. M. CHIA^{2 (b)} and JIAN-XIN ZHU^{1,4 (c)}

¹ *Theoretical Division, Los Alamos National Laboratory, Los Alamos, New Mexico 87545, USA*

² *Division of Physics and Applied Physics, School of Physical and Mathematical Sciences, Nanyang Technological University, 637371 Singapore*

³ *School of Materials Science and Engineering, Nanyang Technological University, 639798 Singapore*

⁴ *Center for Integrated Nanotechnologies, Los Alamos National Laboratory, Los Alamos, New Mexico 87545, USA*

PACS 88.40-J – Types of solar cells

PACS 74.20.Pq – Electronic structure calculations

PACS 71.35.-y – Excitons and related phenomena

PACS 71.45.Gm – Exchange, correlation, dielectric and magnetic response functions, plasmons

Abstract – In the development of highly efficient photovoltaic cells, solid perovskite systems have demonstrated unprecedented promise, with the figure of merit exceeding nineteen percent of efficiency. In this paper, we investigate the optical and vibrational properties of organometallic cubic perovskite $\text{CH}_3\text{NH}_3\text{PbI}_3$ using first-principles calculations. For accurate theoretical description, we go beyond conventional density functional theory (DFT), and calculated optical conductivity using relativist quasi-particle (*GW*) correction. Incorporating these many-body effects, we further solve Bethe-Salpeter equations (BSE) for excitons, and found enhanced optical conductivity near the gap edge. Due to the presence of organic methylammonium cations near the center of the perovskite cell, the system is sensitive to low energy vibrational modes. We estimate the phonon modes of $\text{CH}_3\text{NH}_3\text{PbI}_3$ using small displacement approach, and further calculate the infrared absorption (IR) spectra. Qualitatively, our calculations of low-energy phonon frequencies are in good agreement with our terahertz measurements. Therefore, for both energy scales (around 1.5 eV and 0-20 meV), our calculations reveal the importance of many-body effects and their contributions to the desirable optical properties in the cubic organometallic perovskites system.

Introduction. – Current progress in hybrid perovskite systems have shown significant promise in developing efficient yet low cost photovoltaics [1]. Since the discovery of organometallic perovskite $\text{CH}_3\text{NH}_3\text{PbX}_3$ (X=Cl, Br, I) by Kojima *et al.* [2], there have been several experimental investigations on different phases of these systems. Higher power conversion efficiencies (PCE) have been reported by several groups, which exceeds 12% conversion rate [3, 4]. Recently Heo *et al.* [5] have found 12.3% PCE in $\text{CH}_3\text{NH}_3\text{PbI}_3$ on TiO_2 substrate. The thin films of $\text{CH}_3\text{NH}_3\text{PbI}_3$ have also been reported [6–8] to

have a very high diffusion (about 100 nm) length for both electrons and holes, which makes them excellent candidates for optoelectronic devices. This leads one to believe that excitons may play an important role for energy transfer mechanism in these systems. In addition, there have also been several experimental [9,10] and theoretical [11,12] studies on the structural stability in hybrid perovskite $\text{CH}_3\text{NH}_3\text{PbI}_3$. The high sensitivity of fundamental band gap to various stable crystal-structure phases of $\text{CH}_3\text{NH}_3\text{PbI}_3$ has been reported [11,12], suggesting the importance of the structure stability in both solar-cell applications and optoelectronic devices. More recently, it has also been predicted [13] that the cation-induced structure variability can promote strikingly different electronic and

(a)Corresponding author: atowfiq@lanl.gov

(b)Corresponding author: ElbertChia@ntu.edu.sg

(c)Corresponding author: jxzh@lanl.gov

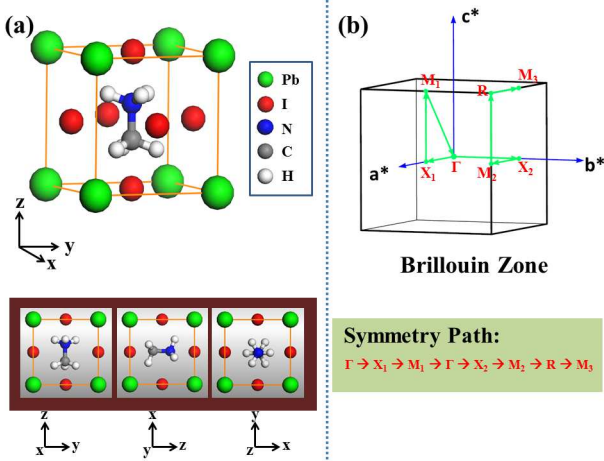


Fig. 1: (Color online) Ionic relaxed crystal structure and Brillouin Zone for the organometallic cubic perovskite $\text{CH}_3\text{NH}_3\text{PbI}_3$; (a) The final optimized configuration of the methylammonium cation in side the cubic cell. Lower panel shows several cross-sectional view along x , y and z axis. (b) The k -paths along high symmetry points, along which the band structure is displayed.

optical properties.

In this Letter, we focus on the excitonic effects on the optical conductivity of cubic $\text{CH}_3\text{NH}_3\text{PbI}_3$ using first-principles methods. The excitons are electron-hole pairs, a phenomenon, which is often found in wide band-gap semiconducting systems. These are associated with bound states formed between the excited electrons and the remaining holes. To capture these excitonic effects, more specifically the Coulomb interaction between the excited electrons and the remaining holes, we go beyond the random-phase approximation (RPA) and DFT-based single particle theory, and solve the equation of motion for two-particle response functions, formally known as Bethe-Salpeter equations (BSE) [14–17]. Due to the presence of significant spin-orbit coupling (SOC) in Pb ions, we also perform calculation using our own generated full-relativistic pseudo-potential, and compare the results with non-relativistic (no SO coupling) calculations. We observe that both SOC and BSE with GW -correction play a significant role in optical properties of $\text{CH}_3\text{NH}_3\text{PbI}_3$ system. We find that the obtained exciton has about 0.153 eV of binding energy for a band gap of 1.48 eV. Our results may provide an alternative interpretation of optical response as measured by photoluminescence spectroscopy [18]. We also calculate the vibrational modes and infrared absorption (IR) spectra based on the ionically relaxed structure of cubic $\text{CH}_3\text{NH}_3\text{PbI}_3$. The modes in the low frequency region are in a qualitative agreement with dominant peak features observed in our THz conductivity measurement on a $\text{CH}_3\text{NH}_3\text{PbI}_3$ thin film.

Computational Details and Experimental Method. – Experimental characterization of the

crystal structure of hybrid perovskites are difficult. The X-ray diffraction on high-quality $\text{CH}_3\text{NH}_3\text{PbI}_3$ crystals has identified cubic, tetragonal, and orthorhombic phases; while the transmission electron microscopy has suggested a pseudo-cubic phase to be consistent with the variability in the octahedral tilting [19]. Throughout the paper, the cubic phase is considered by neglecting small distortions as in Ref. [11]. We perform the first-principles calculations in several steps. We start with a DFT-based structural optimization by relaxing the internal coordinate of the ions in the cubic $\text{CH}_3\text{NH}_3\text{PbI}_3$ unit cells while keeping the lattice constant and cell shape fixed (see Fig. 1(a)). The force on each atom was optimized within 5 meV/Å. For these calculations, we used fixed value of $a = b = c = 6.26$ Å for the lattice constants, which are obtained from the powder diffraction experiment [11, 19].

For the above DFT step, we use *ab initio* package VASP [20] and choose ultra-soft pseudo potentials [21, 22] with PBE exchange correlation functional [23, 24]. The first Brillouin zone (BZ) is sampled with $4 \times 4 \times 4$ k -points using the Monkhorst Pack grid. Once the ionic and electronic relaxations have been achieved, we employ the small-displacement approach to calculate the vibrational eigen-frequencies and eigenvectors. Linear response method is used to calculate the Born effective charge tensors. The infrared-active modes are then obtained by the corresponding oscillator strength [25]:

$$f(\omega_n) = \sum_{\alpha} \left| \sum_{i\beta} Z_{\alpha\beta}^*(i) v_{\beta}(i|\omega_n) \right|^2, \quad (1)$$

where $Z_{\alpha\beta}^*(i)$ is the effective charge tensor of i -th atom, $v_{\beta}(i|\omega_n)$ is the vibrational eigenvector for i -th atom and n -th eigen-frequency ω_n , and α, β are the three components of the cartesian axis. Using these oscillator strengths, we simulate the experimentally observable IR spectra based on a simple analytical expression [26]:

$$I(\omega) = \sum_n f(\omega_n) \delta_m(\omega - \omega_n) / \sum_n f(\omega_n), \quad (2)$$

where $\delta_m(\omega)$ are delta like functions defined by:

$$\delta_m(\omega) = \frac{m}{\pi} \frac{1}{1 + m^2\omega^2}. \quad (3)$$

The broadening of the Lorentzian peaks are adjusted to have the best agreement with experimental data (see Fig. 4).

For the excitonic contribution to the optical conductivity, we perform a single shot GW correction on top of our DFT calculations, and finally solve the BSE as implemented in the code YAMBO [27]. In $\Sigma(\omega) = G^0(\omega)W(\omega)$ self-energy formalism, G^0 stands for the non-interacting Green's function, where W is the screened Coulomb interaction, $W(\mathbf{r}, \mathbf{r}', \omega) = \epsilon^{-1}(\mathbf{r}, \mathbf{r}', \omega)\mathbf{V}(\mathbf{r}, \mathbf{r}')$. Here, $V(\mathbf{r}, \mathbf{r}')$ is the bare Coulomb interaction. The frequency dependent dielectric function $\epsilon(\mathbf{r}, \mathbf{r}', \omega)$ is calculated from the

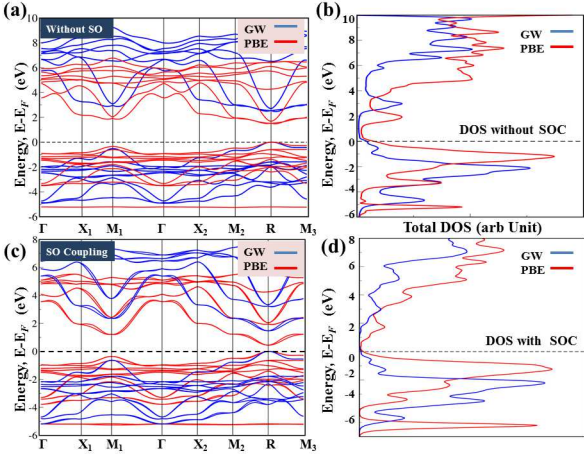


Fig. 2: (Color online) DFT band structure and total DOS with *GW* (solid blue curve) and without *GW* (solid red curve) correction. Top right and left panels ((a) and (b)) show the total DOS and band structure without the SOC. Bottom panels ((c) and (d)) show results with the SOC. Horizontal dashed lines show the location of Fermi energy.

response function $\chi(\omega)$ as [28–31]:

$$\epsilon_{\mathbf{G},\mathbf{G}'}^{-1} = \delta_{\mathbf{G},\mathbf{G}'} + V(\mathbf{q} + \mathbf{G})\chi_{\mathbf{G},\mathbf{G}'}(\mathbf{q},\omega), \quad (4)$$

where within the random phase approximation (RPA) [14, 28], the response function $\chi_{\mathbf{G},\mathbf{G}'}(\mathbf{q},\omega)$ can be calculated from non-interacting χ^0 and Green's function G^0 . The quantity $\mathbf{q} = \mathbf{k} - \mathbf{k}'$ is momentum transfer and \mathbf{G} is the reciprocal lattice vectors. This method was first proposed by Hedin [32], and further details can be found in Refs. [29, 33–37]. It has been found that the inclusion of SOC in the *GW* calculations is also important in *5f*-electron materials [38, 39].

This *GW* method is a many-body perturbation technique which accounts for missing dynamical correlation in the DFT. This *GW*-correction method has been used to successfully predict accurate band gaps for various narrow-gap semiconductors. Therefore, in $\text{CH}_3\text{NH}_3\text{PbI}_3$ system under consideration, we perform *GW* correction on top of the DFT calculations. Convergence of *GW* calculations with respect to various parameters are often nontrivial and necessary to predict the accurate band gap in the wide gap semiconductors and insulators. In this work, we have used one shot *GW* using the Godby-Needs (GN) plasmon-pole model [40] as implemented in Yambo. Previously such GN model was demonstrated to agree very well with the model free *GW* self-energy for predicting band gap in other systems [41]. Using this framework within Yambo, we have achieved the convergence of our *GW* band-structure calculations with 200 bands and 36 momentum transfer \mathbf{q} points in the irreducible Brillouin zone. Furthermore, we have also converged our calculations with respect to polarization matrix dimension and with 200 bands in the evaluation of polarization function. Our *GW* convergence is also performed with respect to the wave function cutoff

energy at the DFT level, for which we have found 70 Ry is sufficient for our system of interest.

However, for systems with larger band gap, the RPA is no longer adequate, and one has to incorporate electron-hole (e-h) correlation in the response function χ . This is the Bethe-Salpeter equation (BSE), where one calculates the response function in terms of the noninteracting two particle e-h Green's function. The details of this formalism can be found in Refs. [14, 15, 27]. Alternatively, one can also solve the BSE by reducing the problem to a two-particle e-h Hamiltonian [14]. The eigenvectors of this Hamiltonian are the excitonic states $|\lambda\rangle$ with E_λ being the corresponding excitonic binding energies within the Tamm-Dancoff [42] approximation, in which only positive energies are considered after diagonalizing the non-Hermitian e-h Hamiltonian [27]. For narrow-gap semiconductors, the effect of BSE is usually negligible; while for wide gap semiconductors, E_λ are often within the gap and can thus have significant contribution to the optical properties. The YAMBO program uses single-particle quantities based on the DFT calculations within the Quantum Espresso (QE) [43]. Therefore, we export the VASP optimized structure to QE and, through the ionic force calculation, verify the optimized structure from the VASP. The relaxed structure is then used to calculate the electronic band-structure and total density of states. We use norm-conserving PBE based pseudopotentials in QE. To account for the SO coupling, we generated fully relativistic norm-conserving PBE pseudopotential by including the 5d semi-core electrons as the valence states for the Pb ions. For both cases (with and without SO coupling), QE generates DFT band-structure, which are then renormalized with *GW* corrections using YAMBO. Finally, excitonic contributions to the optical properties are incorporated on top of DFT and DFT+*GW* calculations including SO coupling. Convergence test on our BSE calculations were performed on equal footing with *GW* calculations. We reached high level of convergence in our estimation of excitonic states by using 80 bands (60 of which are unoccupied) and 36 \mathbf{q} points. Further convergence was tested with respect to polarization bands and matrix dimension. Similar convergence criteria were also reported in previous work [44].

The THz transmission spectra of the $\text{CH}_3\text{NH}_3\text{PbI}_3$ perovskite sample was obtained using Teraview TPS3000 THz time-domain spectrometer, coupled with a Janis ST-100-FTIR cryostat. The perovskite film of thickness 230 nm is deposited on a *z*-cut quartz substrate. A bare substrate is used for the reference run. By fitting the spectra with the thin-film-on-substrate transmission expression, one obtains the complex THz conductivity of the sample. The experimental details are described in Ref. [45]. Data taken at 300 K and 20 K are presented in the present work.

Results. – All our calculations presented in the Letter are based on highly optimized structure of cubic $\text{CH}_3\text{NH}_3\text{PbI}_3$ system. The ionic relaxation are performed

Table 1: Fundamental band gap and lattice parameters in cubic $\text{CH}_3\text{NH}_3\text{PbI}_3$.

	This Work	Other Work	Expt.
$a=b=c$	6.26 Å	–	6.26 Å [19]
$\alpha = \beta = \gamma$	90°	–	
gap (PBE)	1.51 eV	1.38 eV [46]	–
gap (PBE+GW)	2.53 eV	–	–
gap (PBE+SO)	0.46 eV	0.53 eV [46]	–
gap (PBE+SO+GW)	1.48 eV	1.27 eV [46]	1.61 eV [18]
gap (PBE+SO+sc-GW)	–	1.67 eV [46]	1.61 eV [18]

for internal coordinates while we kept the lattice parameters fixed. The final configurations of the atoms are shown in Fig. 1(a). In the lower panel of Fig. 1(a), we show \mathbf{x} , \mathbf{y} , and \mathbf{z} projected cross-sectional view, which shows the final orientation of methylammonium cation inside the cubic cell. For the band structure calculations, we use high symmetry \mathbf{k} -paths inside the first Brillouin zone as shown in Fig. 1(b).

SOC and QP correction. We have systematically studied the effect of SOC as well as GW self-energy corrections on the fundamental band gap of cubic $\text{CH}_3\text{NH}_3\text{PbI}_3$. The PBE-DFT calculations without SOC predicts 1.5 eV gap (solid red line in Fig. 2(a)) while GW correction (without SOC) estimates the gap to be 2.5 eV (solid blue line in Fig. 2(a)). The inclusion of SOC reduced the band gap to be 0.46 eV for DFT (solid red line in Fig. 2(c)) while the GW corrections corrects the band gap up to 1.48 eV (solid blue curve in Fig. 2(c)). The corresponding total density of states (DOS) are shown in Fig. 2(b) and (d). The experimental band gap for this system was found to be 1.61 eV at room temperature [18]. Therefore, we see that the inclusion of SOC underestimates the band gap by more than one eV, while the GW correction without SOC overestimates the gap by about 0.9 eV. Our systematic study reveals that the best agreement with experiment is reached when we include both the SOC and GW self-energy correction. All our calculated values of band gap at various conditions are listed in Table I. We point out that our finding of the effects of SOC and self-energy correction on band gap agree well with earlier results reported by Brivio *et al.* [46] for the cubic phase and by Amat *et al.* [50] for the tetragonal phase of the perovskite. For orthorhombic and tetragonal phase, Zhu *et al.* [44] have reported the band gap correction to be 1.69 eV and 1.57 eV correspondingly using GW and SOC. Umari *et al.* [47] have also reported such band gap around 1.67 eV while the experimental band gap in such systems was determined to be 1.6 eV. We ascribe such a small discrepancy to the fact that various plasmon models have been used for the frequency dependence of the dielectric matrix.

Excitonic Effect. In the presence of SOC, we calculated the dielectric function and optical conductivity by solving BSE without (Fig. 3(a)) and with (Fig. 3(b))

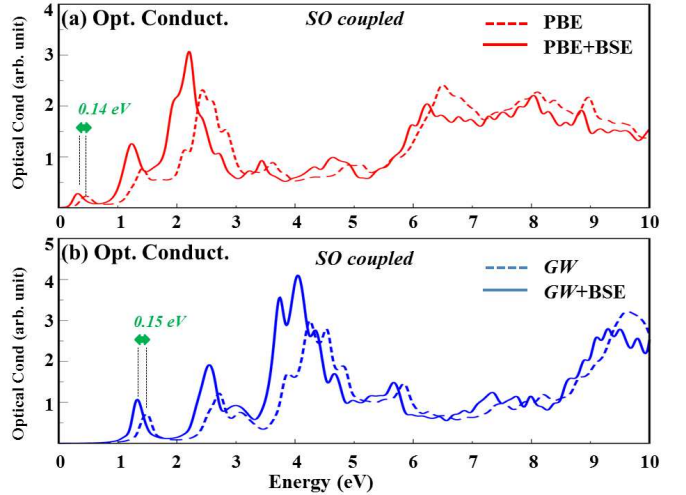


Fig. 3: (Color online) (a) Optical conductivity with BSE (solid red) and without BSE (dashed red) corrections using the DFT calculations; (b) Optical conductivity with BSE (solid blue) and without BSE (dashed blue) using the DFT plus GW self-energy correction. The arrows in both panels (top and bottom) point the excitonic contribution to the optical conductivity. All calculations include SOC.

the self-energy correction. The peaks in optical conductivity represent the electronic excitations from valence band to conduction band satisfying the optical selection rule [48,49]. Therefore, the fundamental gap can be represented by the location of the first peak in optical conductivity spectrum. By incorporating the excitons through the solutions of BSE, we find enhanced peak appearing below the gap edge. These peaks are indicated by the arrows in Fig. 3. We also find that the BSE solutions including GW self-energy correction, as shown in Fig. 3(b), give rise to more pronounced excitonic contribution than without GW correction (Fig. 3(a)). By comparing the location of this shifted excitonic peak with the band gap edge, we are able to deduce that the exciton binding energy is about 0.153 eV. Interestingly, we observed the excitonic binding energy for the cubic phase is larger than for the tetragonal or orthorhombic phase reported earlier in literature [44]. Experimentally, it is important to find out the implica-

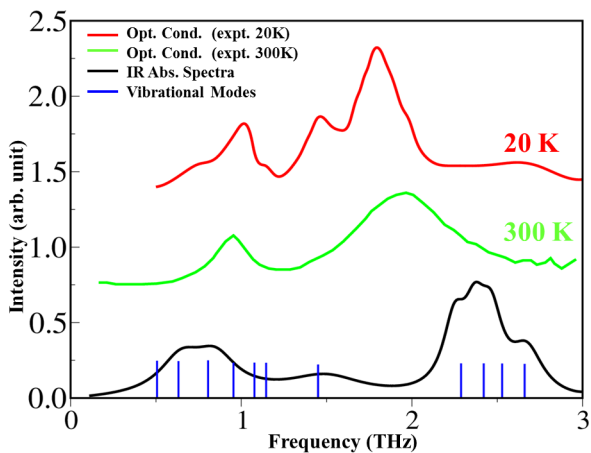


Fig. 4: (Color online) Vibration mode and optical spectra. The top curves (solid red and green) represent experimental data for terahertz conductivity on a $\text{CH}_3\text{NH}_3\text{PbI}_3$ thin film. The bottom curve (black) is the calculated infrared absorption spectrum. Vertical blue lines are the location of vibrational mode frequencies.

tion of a higher binding energy of excitons to the long diffusion length observed in perovskite thin films or heterostructures, where the strain effect from the substrate or sandwiching materials may play an important role.

Vibrational Modes vs. Measurements. The presence of flexible methylammonium cation at the center of the rigid perovskite cage implies that the crystal structure of this organometallic compound is softer than that of transition metal oxide perovskite with the former having expanded lattice constants. This observation motivates us to investigate the vibrational modes, which can be probed by low-frequency spectroscopy such as Raman, IR, or THz conductivity. For this purpose, the vibrational mode energy and oscillator strength are calculated. The IR spectra are simulated with a Lorentzian fitting. The results are shown in Fig. 4, with the vertical blue lines denoting the positions of vibrational mode frequencies. We see that our calculated IR absorption spectra, as represented by the solid black curve, reproduces qualitatively similar peak features observed in experimental data for the THz conductivity (red and green lines), in the low frequency region (0-3 THz). The computed spectra is slightly stretched in the frequency range. Such stretch has also been reported by earlier *ab initio* calculations of Raman spectra for $\text{CH}_3\text{NH}_3\text{PbI}_3$ [51]. Our THz conductivity measurement demonstrates the possible energy and charge transfer mechanism in cubic $\text{CH}_3\text{NH}_3\text{PbI}_3$ through the low-energy vibrational phonon modes.

Conclusion. – In summary, we have demonstrated the effect of excitons and vibrational modes on the optical properties of cubic organometallic perovskite $\text{CH}_3\text{NH}_3\text{PbI}_3$. All our calculations have been based on internally relaxed stable ionic structure with the experi-

mental lattice parameters. Our study has uncovered the importance of both the SOC and quasi-particle self-energy correction, which conspire to reproduce the experimentally observed fundamental band gap. In this wide-gap semiconductor, we have found significant excitonic contribution to the optical conductivity at about ~ 1.5 eV using first-principles BSE calculations. In addition, we have also performed first-principles simulations of the vibrational modes due to the presence of flexible methylammonium cations at the center of the cubic perovskite cage. We have shown that the signature of the modes can be revealed in the IR spectra, with the profile very similar to the THz conductivity we have measured on a $\text{CH}_3\text{NH}_3\text{PbI}_3$ thin film. Therefore, our first-principles calculations have predicted that the features of the excitation spectra must originate from the strong SOC, many-body effects, and low-energy vibrational modes. Our systematic first-principles study, for the first time, has benchmarked the various competing effects, which must be taken into account to understand and utilize the optoelectronic properties of $\text{CH}_3\text{NH}_3\text{PbI}_3$ to enhance its solar-cell applications.

We thank M. J. Graf, Amanda Nuekirch, Carl Greef, Davide Sangalli, A. Walsh, and B. Xiao for useful discussions. This work was supported by U.S. DOE at LANL under Contract No. DE-AC52-06NA25396 and the LANL LDRD Program (T.A. & J.-X.Z.), and Singapore Ministry of Education AcRF Tier 1 (RG 13/12 & 2014-T1-001-056) and the National Research Foundation Competitive Research Programme (NRF-CRP4-2008-04) (E.E.M.C.), and the Danish Council for Strategic Research (Y.M.L.). The work was supported in part by the Center for Integrated Nanotechnologies, a U.S. DOE BES user facility.

REFERENCES

- [1] LOI M. A. and HUMMELEN J. C., *Nat. mater.*, **12** (2013) 1087.
- [2] KOJIMA A., TESHIMA K., SHIRAI Y., and MIYASAKA T., *J. Am. Chem. Soc.*, **131** (2009) 6050.
- [3] BURSCHKA J. *et al.*, *Nature*, **499** (2013) 316.
- [4] LIU M. *et al.*, *Nature*, **501** (2013) 395.
- [5] HEO J.H. *et al.*, *Nat. Photonics*, **7** (2013) 486.
- [6] STRANKS S. D. *et al.*, *Science*, **342** (2013) 341.
- [7] XING G. *et al.*, *Science*, **342** (2013) 344.
- [8] SUN A. *et al.*, *Energy Environ. Sci.*, **7** (2014) 399.
- [9] NIU G. *et al.*, *J. Mater. Chem. A*, **2** (2014) 705.
- [10] KAWAMURA Y. *et al.*, *J. Phys. Soc. Jap.*, **71** (2002) 1694.
- [11] BRIVIO F., WALKER A. B., and WALSH A., *Applied Phys. Lett. Mater.*, **1** (2013) 042111.
- [12] FENG J. and XIAO B., *J. Phys. Chem. Lett.*, **5** (2014) 1278.
- [13] AMAT A. *et al.*, *Nano Lett.*, **14** (2014) 3608.
- [14] ONIDA G., REINING L., and RUBIO A., *Rev. Mod. Phys.*, **74** (2002) 601.
- [15] STRINATI G., *Phys. Rev. B.*, **29** (1984) 5718.

- [16] HYBERTSEN M. S. and LOUIE S. G., *Phys. Rev. B*, **34** (1986) 5390.
- [17] ALBRECHT A., ONIDA G., and REINING L., *Phys. Rev. B*, **55** (1997) 10297.
- [18] YAMADA Y. *et al.*, *Appl. Phys. Express*, **7** (2014) 032302.
- [19] BAIKIE T. *et al.*, *J. Mater. Chem. A*, **1** (2013) 5628.
- [20] KRESSE G. and FURTHMÜLLER J., *Phys. Rev. B*, **54** (1996) 11169.
- [21] VANDERBILT D., *Phys. Rev. B*, **41** (1990) 7892.
- [22] KRESSE G. and HAFNER J., *J. Phys.: Condens. Matter*, **6** (1994) 8245.
- [23] PERDEW J. P., BURKE K., and ERNZERHOF M., *Phys. Rev. Lett.*, **77** (1996) 3865.
- [24] PERDEW J. P., BURKE K., and ERNZERHOF M., *Phys. Rev. Lett.*, **78** (1997) 1396.
- [25] BRÜESCH P., *Phonons: Theory and Experiments II* (Springer, Berlin) 1986.
- [26] TAO J., TRETIAK S., and ZHU J.-X., *J. Phys. Chem. B*, **112** (2008) 13701.
- [27] MARINI A. *et al.*, *Comput. Phys. Commun.*, **180** (2009) 1392.
- [28] HEDIN L. and LUNDQVIST S., *Solid State Phys.*, **23** (1969) 1.
- [29] HEDIN L., *J. Phys.: Condens. Matter*, **11** (1999) R489.
- [30] LEE J. D., GUNNARSSON O., and HEDIN L., *Phys. Rev. B*, **60** (1999) 8034.
- [31] HEDIN L. and LUNDQVIST S., *Solid State Physics*, edited by SEITZ F., TURNBULL D., EHRENREICH H. (Academic, New York) 1969, pp. 1-181.
- [32] HEDIN L., *Phys. Rev.*, **139** (1965) A796.
- [33] ARYASETIAWAN F. and GUNNARSSON O., *Rep. Prog. Phys.*, **61** (1998) 237.
- [34] STRINATI G. and MATTAUSCH H. J. and HANKE W., *Phys. Rev. B*, **25** (1982) 2867.
- [35] ALBUR W. G., JÖNSSON L., and WILKINS J. W., *Solid State Physics*, **54** (2000) 1.
- [36] INKSON J. C., *Many-body Theory of Solids* (Plenum Press) 1984, p. 325.
- [37] KOTANI T., and VAN SCHILFGAARDE M., *J. Phys.: Condens. Matter*, **20** (2008) 295214.
- [38] KUTEPOV A., HAULE K., SAVRASOV S. Y., and KOTLIAR G., *Phys. Rev. B*, **85** (2012) 155129.
- [39] AHMED T., ALBERS R. C., BALATSKY A. V., FRIEDRICH C., and ZHU J. X., *Phys. Rev. B*, **89** (2014) 035104.
- [40] GODBY R. W. and NEEDS R. J., *Phys. Rev. Lett.*, **62** (1989) 1169.
- [41] STANKOVSKI M. and ANTONIUS G. and WAROQUIERS D. and MIGLIO A. and DIXIT H. and SANKARAN K. and GIANTOMASSI M. and GONZE X. and CÔTÉ M. and RIGNANESE G.-M., *Phys. Rev. B*, **84** (2011) 241201.
- [42] FETTER A. L. and WALECKA J. D., *Quantum Theory of Many-Particle Systems* (McGraw-Hill, Inc., New York) 1971.
- [43] GIANNOZZI P. *et al.*, *J. Phys.: Condens. Matter*, **21** (2009) 395502.
- [44] ZHU X. and SU H. and MARCUS R. A. and MICHEL-BEYERLE M. E., *J Phys. Chem Lett.*, **5** (2014) 3061.
- [45] ZOU X. *et al.*, *Phys. Rev. Lett.*, **110** (2013) 067401.
- [46] BRIVIO F., BUTLER K. T., WALSH A., and VAN SCHILFGAARDE M., *Phys. Rev. B*, **89** (2014) 155204.
- [47] UMARI P. and MOSCONI, E. and ANGELIS F. D., *Scientific Reports*, **4** (2014) 4467.
- [48] EBERHARDT W. and HIMPEL F. J., *Phys. Rev. B*, **21** (1980) 5572.
- [49] ZHU B., *Phys. Rev. B*, **37** (1988) 4689.
- [50] AMAT A. and MOSCONI E. and RONCA E. and QUARTI C. and UMARI P. and NAZEERUDDIN M. K. and GRITZEL M. and DE ANGELIS F., *Nano Lett.*, **14** (2014) 3608.
- [51] QUARTI C. *et al.*, *J. Phys. Chem. Lett.*, **5** (2014) 279.